

## FAST MODES AND DUSTY HORSESHOES IN TRANSITIONAL DISKS

TUSHAR MITTAL<sup>1</sup> AND EUGENE CHIANG<sup>1,2</sup>*Draft version December 9, 2014*

## ABSTRACT

The brightest transitional protoplanetary disks are often azimuthally asymmetric: their mm-wave thermal emission peaks strongly on one side. Dust overdensities can exceed  $\sim 100:1$ , while gas densities vary by factors less than a few. We propose that these remarkable ALMA observations—which may bear on how planetesimals form—reflect a gravitational global mode in the gas disk. The mode is (1) fast—its pattern speed equals the disk’s mean Keplerian frequency; (2) of azimuthal wavenumber  $m = 1$ , displacing the host star from the barycenter; and (3) Toomre-stable. We solve for gas streamlines including the indirect stellar potential in the frame rotating with the pattern speed, under the drastic simplification that gas does not feel its own gravity. Near co-rotation, the gas disk takes the form of a horseshoe-shaped annulus. Dust particles with aerodynamic stopping times much shorter or much longer than the orbital period are dragged by gas toward the horseshoe center. For intermediate stopping times, dust converges toward a  $\sim 45^\circ$ -wide arc on the co-rotation circle. Particles that do not reach their final accumulation points within disk lifetimes, either because of gas turbulence or long particle drift times, conform to horseshoe-shaped gas streamlines. Our mode is not self-consistent because we neglect gas self-gravity; still, we expect that trends between accumulation location and particle size, similar to those we have found, are generically predicted by fast modes and are potentially observable. Unlike vortices, global modes are not restricted in radial width to the pressure scale height; their large radial and azimuthal extents may better match observations.

**Keywords:** protoplanetary disks — accretion, accretion disks — hydrodynamics — celestial mechanics

## 1. INTRODUCTION

Transitional protoplanetary disks possess inner cavities nearly devoid of dust (e.g., Espaillat et al. 2014). Outside these cavities, in some of the brightest disks, radio images reveal that dust is not axisymmetric, but clumps strongly to one side. At dust continuum wavelengths, surface brightness contrasts range from values on the order of a few (Brown et al. 2009; Tang et al. 2012; Isella et al. 2013; Pérez et al. 2014) to  $\sim 30$  (HD 142527; Casassus et al. 2013; Fukagawa et al. 2013) to  $\sim 130$  (Oph IRS 48; van der Marel et al. 2013; Bruderer et al. 2014). These contrasts are lower bounds where observations are unresolved. Unlike dust, overdensities in CO gas are limited to factors of a few at most (van der Marel et al. 2013; Bruderer et al. 2014; Pérez et al. 2014b).

The lopsided dust concentrations—which may be giving us a first empirical glimpse into the process of planetesimal formation—cry out to be understood. One proposed mechanism is dust trapping by gas vortices (e.g., Lyra & Lin 2013; Zhu & Stone 2014). The inner rims of transitional disks may be subject to the Rossby wave instability which can spawn anticyclonic vortices (e.g., Lovelace & Romanova 2014). Whether vortices are radially and azimuthally large enough to match the imaging data is debatable.

We submit here a different explanation, one that follows from a simple fact: a lopsided disk moves the barycenter away from the host star. The gravitational potential therefore includes an “indirect” term (e.g.,

Murray & Dermott 1999). Our paper solves for gas streamlines including the indirect potential, in the limit that gas does not feel its own gravity. We will discover in this limit that gas occupies a radially wide, horseshoe-shaped annulus that readily concentrates dust grains into patterns similar to those observed. Concentration is by gas drag, not dust self-gravity.

Our proposal is that the gas disk exhibits a global “fast” mode of azimuthal wavenumber  $m = 1$ , whose lopsidedness shifts the barycenter off the star. “Fast” means that the disk’s pattern speed equals its mean Keplerian motion, not the apsidal precession frequency that characterizes  $m = 1$  “slow” modes (cf. Tremaine 2001). Fast modes are more attractive than slow modes for shaping dust grain trajectories and explaining the radio observations, since the non-inertial forces arising from a slow mode’s pattern speed are too small to compete with the substantial gas drag forces felt by dust.

We compute gas streamlines (test particle orbits) analytically in §2 and numerically in §3. How dust concentrates aerodynamically is described in §4. Limitations of our calculations—notably our neglect of gas self-gravity, which prevents us from computing fast modes self-consistently—are discussed in §5.

## 2. TEST PARTICLE DYNAMICS

We consider analytically the dynamics of a test particle in the gravitational potential of a star with a prescribed motion. The star has mass  $M_*$  and executes a circular orbit of radius  $\mu$  with fixed angular frequency  $\Omega$  about the origin (star-disk barycenter). This orbit represents the star’s “reflex motion” in response to the  $m = 1$  component of the disk’s potential. We work in the frame rotating with the star and centered on the origin (Figure 1). In our unit system, the gravitational constant

<sup>1</sup> Department of Earth and Planetary Science, 307 McCone Hall, University of California, Berkeley, CA 94720-4767

<sup>2</sup> Department of Astronomy, 501 Campbell Hall, University of California, Berkeley, CA 94720-3411

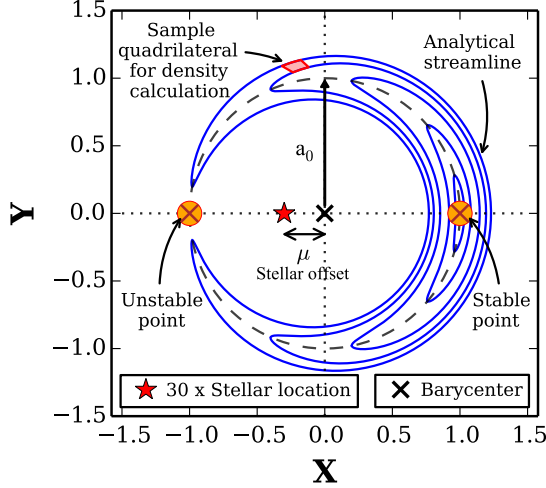


**Figure 1.** In the offset stellar potential, closed and non-crossing orbits take the form of horseshoes enclosing the stable point, and are plotted here using equation (14) for  $B = \{0.02, 0.12, 0.4, 0.7, 0.99\}$ . We show a sample quadrilateral used to construct the gas density.

times the stellar mass  $GM_* = 1 - \mu$ ,  $\Omega = 1$ , and  $\mu \ll 1$ . Our problem is identical to the standard restricted three-body problem, except that the test particle does not feel the gravity of the secondary (read: disk). Because we assume the star’s motion arises from the disk potential but neglect the latter when computing the test particle’s motion, our calculations are not self-consistent; we proceed anyway in the hope that some of the grosser, qualitative features of our model will survive a more careful study.

In Cartesian coordinates, the test particle obeys

$$\ddot{x} - 2\Omega\dot{y} = \frac{\partial U}{\partial x} \quad (1)$$

$$\ddot{y} + 2\Omega\dot{x} = \frac{\partial U}{\partial y} \quad (2)$$

where  $U$  is the celestial mechanician’s centrifugal potential plus the potential of the star (offset from the origin by  $\mu$  on the negative  $x$ -axis):

$$U = \frac{\Omega^2}{2}(x^2 + y^2) + \frac{1 - \mu}{\sqrt{(x + \mu)^2 + y^2}}. \quad (3)$$

Equilibrium points, where gravity and centrifugal forces balance, lie along the  $x$ -axis. Setting  $\ddot{x} = \ddot{y} = \dot{x} = \dot{y} = y = 0$  in equations (1) and (2), we find

$$\frac{\partial U}{\partial x} = x_{\text{eq}} - \frac{(x_{\text{eq}} + \mu)(1 - \mu)}{|x_{\text{eq}} + \mu|^3} = 0. \quad (4)$$

To order  $\mu$ , the two equilibrium points are located at

$$x_{\text{eq}} = 1 - \mu \text{ and } -1 - \mu/3. \quad (5)$$

Assuming that small displacements about these equilibria evolve with time  $t$  according to  $\exp(\lambda t)$ , we linearize and combine equations (1) and (2) to arrive at the relation for the eigenfrequency  $\lambda$ :

$$\lambda^4 + \left[2 - \frac{1 - \mu}{(x_{\text{eq}} + \mu)^3}\right]\lambda^2 + \left[1 + \frac{1 - \mu}{(x_{\text{eq}} + \mu)^3} - 2\frac{(1 - \mu)^2}{(x_{\text{eq}} + \mu)^6}\right] = 0. \quad (6)$$

The equilibrium point at  $x_{\text{eq}} < 0$  is unstable ( $\text{Re } \lambda > 0$ ). By contrast, the equilibrium point at  $x_{\text{eq}} = 1 - \mu$  is stable for  $\mu < 1/10$  and is characterized by two frequencies of oscillation: one nearly equal to the mean motion  $\Omega$  (and representing the usual epicyclic motion of an eccentric orbit), and another

$$|\lambda| = \sqrt{3\mu}\Omega. \quad (7)$$

This slower frequency describes the libration of the particle on trajectories that are shaped like horseshoes. To sketch these horseshoes, we switch to polar coordinates where the equations of motion read

$$\ddot{r} - r\dot{\theta}^2 - 2\Omega r\dot{\theta} = \frac{\partial U}{\partial r} \quad (8)$$

$$r\ddot{\theta} + 2\dot{r}\dot{\theta} + 2\Omega\dot{r} = \frac{1}{r}\frac{\partial U}{\partial \theta} \quad (9)$$

with

$$U = \frac{\Omega^2}{2}r^2 + \frac{1 - \mu}{\sqrt{r^2 + \mu^2 + 2r\mu\cos\theta}} \quad (10)$$

$$\simeq \frac{3}{2} + \frac{3}{2}\Delta^2 - \mu(1 + \cos\theta). \quad (11)$$

In equation (11), we have expanded  $U$  in small radial (but not small azimuthal) displacements  $\Delta \equiv r - 1$  about the stable point. We insert (11) into (8) and (9), keeping only leading-order terms and taking  $d/dt \ll \Omega$  to filter out fast epicycles; then

$$-2\dot{\theta} = 3\Delta \quad (12)$$

$$\ddot{\theta} = -6\mu\frac{\partial}{\partial\theta}\sin^2(\theta/2). \quad (13)$$

Multiplying (13) by  $\dot{\theta}$ , integrating over time, and substituting (12), we obtain the following “shape function”:

$$\Delta^2 = \frac{16}{3}\mu[B - \sin^2(\theta/2)]. \quad (14)$$

Here  $B$  is a constant of integration that takes values between 0 (zero amplitude libration at  $\theta = 0$ ) and 1 (maximal libration). Figure 1 samples several  $B$ -values; evidently the shape function (14) traces horseshoe-shaped trajectories enclosing the stable point. The horseshoes are radially widest at  $\theta = 0$ :

$$\max \Delta = \sqrt{\frac{16B\mu}{3}}. \quad (15)$$

This width can be a large fraction of the radius; e.g., for  $B = 1$  and  $\mu = 0.01$  (characteristic of a disk whose mass is  $\sim 0.01 M_*$ ), the full width is  $2\max \Delta = 0.46$ .

Although the libration trajectories are shaped like horseshoes, the square-root scalings in (7) and (15) for the libration frequency and width characterize tadpoles in the standard three-body problem. This kinship between our horseshoe orbits and conventional tadpoles is expected. In both types of motion, the turning points (located farthest from the positive  $x$ -axis) are effected by the offset host star which exerts torques on the test particle that deflect it back toward the  $x$ -axis.

### 3. CONSTRUCTING A MODEL GAS DISK

We construct a model gas disk based on ideas developed by Paczynski (1977) and applied in many galactic contexts (e.g., Binney et al. 1991; Chang et al. 2007). Gas is assumed to occupy closed, non-intersecting test particle orbits. Crossing orbits are forbidden because they lead to shocks and energy dissipation. Gas streamlines approximate test particle orbits insofar as gas sound speeds are smaller than orbital velocities and gas self-gravity is negligible.

Working in the rotating frame of §2, we set  $\mu = 0.01$ ,  $M_* = M_\odot$ , and  $\Omega = \sqrt{GM_\odot/a_0^3}$ , where  $a_0 = 100$  AU is the disk's characteristic radius. The star is positioned at  $x_* = -\mu a_0 = -1$  AU and  $y_* = 0$ . Starting on the  $x$ -axis, we launch a test particle with an initial velocity  $\dot{y} < 0$  ( $\dot{x} = 0$ ) and integrate its trajectory until it re-crosses the  $x$ -axis. The final position and velocity are required to match initial values to within 1 part in  $10^4$ ; the initial  $\dot{y}$  is varied until these conditions are met. The integrations are performed using Python's explicit Runge-Kutta integrator of order 8(5,3) (dop853) with an accuracy setting of  $10^{-8}$ . A total of 22 initial  $x$ -positions, distributed between the stable point at  $x = x_{\text{eq}} = 99.3$  AU and  $x = x_{\text{max}} = 127.4$  AU are selected for the construction of 22 orbits/streamlines; see Figure 2. Their shapes match well the horseshoe orbits found analytically in §2. In particular, we confirm that equations (7) and (15) for the libration frequency and radial width are obeyed.

Each streamline is defined by  $N = 300$  points marking the test particle's position recorded at equal intervals of time. To compute the gas surface density, we assign each streamline a mass  $\propto \cos[(\pi/2)(x - x_{\text{eq}})/(x_{\text{max}} - x_{\text{eq}})]$ , where  $x$  identifies the streamline's starting position; we assign more mass to inner horseshoes than outer ones. Lines are drawn between adjacent points on neighboring streamlines so that the entire space is tiled by quadrilaterals (see Figure 1). Each quadrilateral of area  $dA$  is assigned a surface density  $\Sigma = dM/dA$ , where  $dM = \text{streamline mass} / N$ .

For the most part this procedure yields surface densities that vary smoothly from quadrilateral to quadrilateral. However, we find a few spikes in density near the disk's edges (outermost horseshoes). These are numerical artifacts that arise from our particular choice of streamlines. Because our gravitational potential is only weakly non-axisymmetric, it admits a large variety of orbits that satisfy our tolerance criteria for being closed and non-intersecting. Our selection of streamlines is thus not unique. We chose streamlines that seemed to minimize the high density spikes, but were not able to eliminate them. Fortunately the afflicted regions, which are restricted to disk edges, are tiny and easily masked out.

We smooth  $\Sigma$  by first applying the Python function `scipy.ndimage.interpolation.map_coordinates` which sub-samples to a finer non-regular  $r$ - $\theta$  grid using a local order-1 spline. We then establish  $\Sigma$  on a regular  $r$ - $\theta$  grid with `scipy.interpolate.griddata` which uses a local linear interpolation. The final step is to normalize the disk mass so that the barycenter remains at the origin. Figure 2 shows our final gas disk, of mass  $M_{\text{disk}} = 0.028 M_\odot$ .

To 0th order, the gas velocities are the (interpolated) velocities of the test particles used to construct the orig-

inal 22 streamlines. We add a 1st order correction to account for gas pressure gradients. With a fractional error of  $\sqrt{\mu}$ , pressure forces are balanced by Coriolis forces (the flow is geostrophic); the velocity corrections read

$$v_{r,1} = -\frac{c_s^2}{2\Omega r} \frac{\partial \ln \Sigma}{\partial \theta} \quad (16)$$

$$v_{\theta,1} = \frac{c_s^2}{2\Omega} \frac{\partial \ln \Sigma}{\partial r} \quad (17)$$

and are evaluated by applying Python's `gradient` function to  $\Sigma$ . Minor numerical artifacts in the 1st order velocities at disk edges are smoothed using a combination of median and Gaussian filters. The sound speed  $c_s$  is fixed at 0.37 km/s, appropriate for gas at 40 K.

### 4. DUST IN GAS

We now add dust particles to our gas disk. A dust particle behaves like a test particle except that it also feels a gas drag acceleration  $-(\mathbf{v}_d - \mathbf{v}_g)/t_{\text{stop}}$  which damps dust-gas relative velocities over an aerodynamic stopping time  $t_{\text{stop}}$ . The stopping time scales inversely as the volumetric gas density  $\rho$ , which we compute from  $\Sigma$  by assuming the disk has a constant vertical thickness  $h = c_s/\Omega$ . Our convention is to assign every particle a Stokes parameter  $\text{St} \equiv \Omega t_{\text{stop}}$  evaluated at the position of peak  $\rho$  (i.e., at the stable point  $x = x_{\text{eq}}$ ,  $y = 0$ ); the stopping time at any other location then scales inversely as the local  $\rho$  (which deviates from the peak value by at most a factor of  $\sim 3$ ). A total of 2100 dust particles are laid down with an initial surface density matching that of the gas disk and with initial velocities equal to the 0th order gas velocities. Dust trajectories are computed using the same Runge-Kutta integrator as was used to obtain the gas streamlines. Gas densities and velocities are computed by local linear interpolation.

Figure 3 shows the evolution of dust surface density for  $\text{St} = 0.01$ , 0.1, and 1 (equivalent to grain sizes of  $\sim 1$  mm, 1 cm, and 10 cm for an assumed bulk density of  $1 \text{ g/cm}^3$ ). Because gas feels pressure forces while dust does not, dust and gas velocities generally differ. Dust particles feel tailwinds/headwinds that drag them toward gas pressure maxima (e.g., Chiang & Youdin 2010). For our disk, the global pressure maximum is located at the stable point, and indeed particles with  $\text{St} = 0.01$  and 0.1 collect there. We estimate the concentration time as follows. In a gas disk with a radial pressure gradient, the radial speed of a particle is

$$v_{\text{dust},r} \sim \frac{c_s^2}{\Omega r} \frac{\partial \ln \Sigma}{\partial \ln r} \frac{\text{St}}{1 + \text{St}^2} \quad (18)$$

valid for any  $\text{St}$  (e.g., Nakagawa et al. 1986). For our problem,  $\partial \ln \Sigma / \partial \ln r \sim \pm 1 / \sqrt{16\mu/3}$  for streamlines to the left/right of the stable point (see Figure 3); we have here used the fact that our disk has a characteristic radial width  $\sqrt{16\mu/3} a_0$  (equation 15). Thus particles interior/exterior to the stable point drift radially outward/inward, traversing a series of ever-smaller horseshoes. The timescale to cross the radial width of the disk and collect onto the stable point is then

$$t_{\text{conc}} \sim \frac{\sqrt{16\mu/3} a_0}{v_{\text{dust},r}} \sim \frac{16}{3} \frac{\mu}{\Omega} \left( \frac{\Omega a_0}{c_s} \right)^2 \frac{1 + \text{St}^2}{\text{St}}. \quad (19)$$

## Gas Surface Density

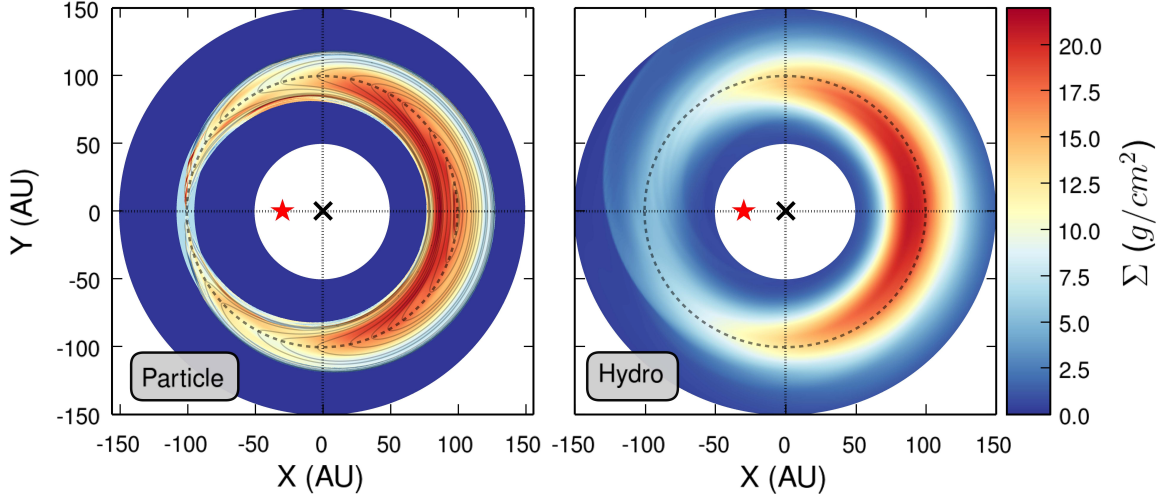


**Figure 2.** *Left:* Gas surface density computed with our test-particle method, for  $\mu = 0.01$ ,  $a_0 = 100$  AU (dashed circle), and  $M_{\text{disk}} = 0.028M_{\odot}$ . Test particle orbits are overlaid as contours. The Toomre parameter  $Q = c_s\Omega/\pi G\Sigma \sim 2-4$  for a sound speed  $c_s \approx 0.37$  km/s (temperature 40 K). Across the horseshoe-shaped annulus,  $\Sigma$  varies by factors  $\lesssim 3$ . *Right:* Gas surface density computed with the hydrocode PLUTO, using parameters identical to those in panel (a). We use a polar grid that spans  $0$  to  $2\pi$  in azimuth and  $0.2a_0$  to  $2a_0$  in radius; a grid resolution of  $400 \times 400$  cells; outflow boundary conditions; and an isothermal  $c_s = 0.37$  km/s. Initially the disk is centered on the origin (frame rotation axis), extends from  $0.9a_0$  to  $1.1a_0$ , and has uniform density. The snapshot is taken after 80 orbits (evaluated at  $a_0$ ), with qualitatively similar results from 20–80 orbits; at earlier times, strong transients afflict the disk, and at later times, the disk has lost much of its mass through the outer boundary. We are encouraged by the agreement between the test-particle and hydrocode methods.

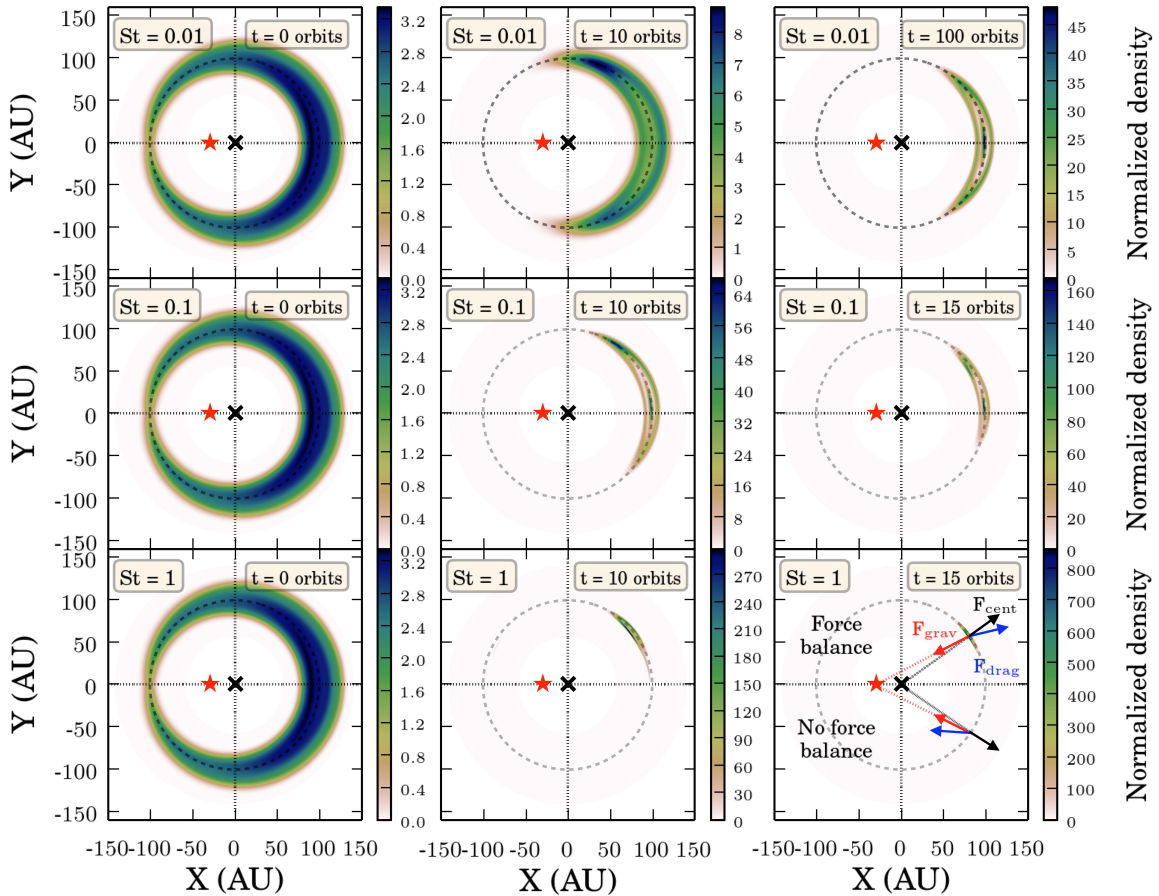


**Figure 3.** How dust surface density varies with time (left to right) and Stokes parameter (top to bottom). Since our gas disks are not turbulent, all dust grains of a given size eventually collect to a point. The location of this point varies with grain size; see also Figure 5. For  $St = 1$ , the collection point is displaced from the usual stable equilibrium by about  $+45^\circ$ ; here drag (which points radially outward because  $\partial\Sigma/\partial\theta < 0$  in equation 16) can balance gravity and centrifugal forces. Adding a turbulent diffusivity  $\alpha$  can keep dust patterns more spatially extended (§5).

which predicts that  $St \sim 1$  particles accumulate fastest. Our numerical experiments confirm this expectation and also verify the asymptotic scalings ( $t_{\text{conc}} \propto 1/St$  for  $St \lesssim 0.1$  and  $t_{\text{conc}} \propto St$  for  $St \gtrsim 4$ ; see Figure 4).

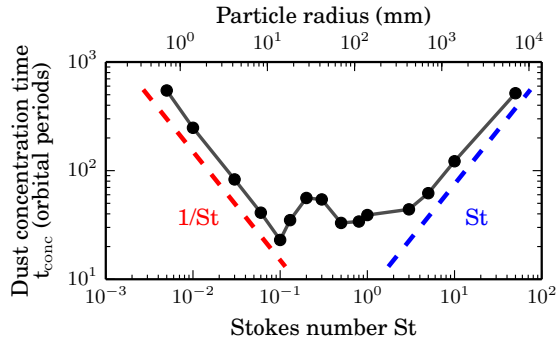


**Figure 4.** Dust concentration timescales (defined as the time for dust that is initially well-mixed with gas to collect into a region subtending  $4^\circ$  in azimuth). These simulation results confirm the asymptotic scalings predicted by equation (19) for  $St \ll 1$  and  $St \gg 1$ .

Surprisingly, not all particles concentrate at the global pressure maximum located on the  $x$ -axis (the gas disk symmetry axis). Figures 3 and 5 reveal that marginally aerodynamically coupled particles collect along an arc that extends off the  $x$ -axis in the direction of orbital motion. Starting from the  $x$ -axis at  $St \lesssim 0.1$ , the position angles of final accumulation points advance with increasing  $St$  to a maximum of  $\sim 45^\circ$  at  $St \approx 0.5$ ; further increasing  $St$  causes the position angles to slide back down, returning to zero at  $St \gtrsim 10$ . The bottom right panel of Figure 3 illustrates that, as long as the drag force is neither too strong nor too weak, a three-way force balance between the offset stellar gravity, the centrifugal force, and drag is possible, but only in one quadrant of the rotating frame. Particle size segregation off-axis offers an observational test of our model: the locations of peak intensity in dust emission maps may vary systematically with wavelength, to the extent that different observing wavelengths select for different size particles.

## 5. DISCUSSION AND FUTURE DIRECTIONS

A lopsided disk displaces its host star from the system barycenter. In the resultant “offset” stellar potential (one that has an indirect term), we have calculated that gas streamlines take the form of horseshoes. Our calculations are not self-consistent because on the one hand we have invoked the gas disk’s mass to move the star, but on the other we have neglected the disk’s gravity when computing gas streamlines. Our neglect of gas self-gravity is a severe approximation: the disk’s gravity is as strong as the indirect forcing, since both scale as  $\mu$ . Indeed, when we re-calculate *a posteriori* the potential  $U$  including the gas disk’s contribution, we find that  $U$ ’s topology changes qualitatively. In particular, what was a global extremum at  $x = x_{\text{eq}}$  becomes a saddle point. Thus the mode we have constructed in this paper is not an equilibrium fast mode. Still, we might not be too far off the mark; reducing the disk mass by a factor of  $\sim 2$  (while keeping the stellar offset  $\mu$  fixed) restores the original topology at  $x_{\text{eq}}$ . We are also encouraged by stellar dynamics calculations performed by Dury et al. (2008),

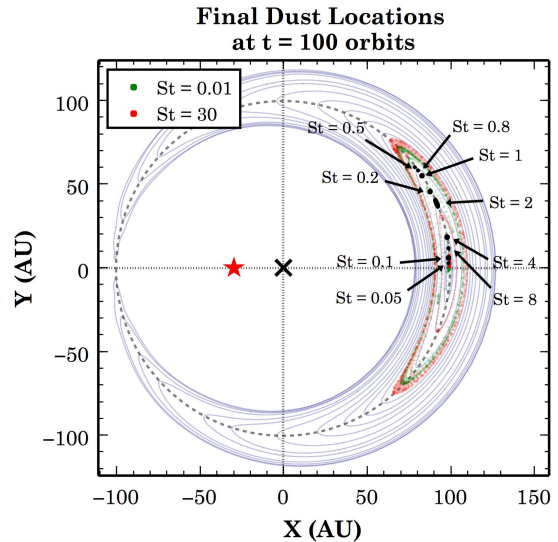


**Figure 5.** Final accumulation points for dust particles with various  $St$  numbers. The collection points advance in azimuth from  $St = 0.05$  to  $0.5$ , and then move back down from  $St = 0.5$  to  $8$ . Depending on the dust size distribution, this systematic variation might be observable by imaging the disk at multiple wavelengths. Particles with  $St = 0.01$  and  $30$  have yet to converge to the stable point at the end of 100 orbits when this snapshot was taken.

who found that their “rotating lopsided mode” (i.e., a fast  $m = 1$  mode) supports “banana” (i.e., horseshoe-shaped) orbits; see their Figure 14. Future work should incorporate disk self-gravity, not only to construct self-consistent fast modes, but also to search for instabilities that can create lopsided mass distributions.

One step toward more realistic gas equilibria is to replace our test-particle calculation with a hydrodynamical one that accounts for gas pressure. In this regard, we experimented with a 2D inviscid hydro-simulation using the PLUTO code (Mignone et al. 2007), evolving an initially circular and uniform gas ring in an offset stellar potential (see caption to Figure 2b for technical details). A few numerical difficulties complicated this first-cut experiment. The system did not settle into steady state; gas leaked outward and was lost off the grid; and our boundary conditions, chosen mainly for convenience, affected the propagation of spiral density waves. Nevertheless,  $\sim 20$ – $80$  orbits into our hydro-simulation, we observed the gas disk conforming to the same horseshoe shapes obtained with our test-particle method—compare Figures 2a and 2b—and found consistent results for dust concentration. The qualitative agreement between our test-particle calculation and our hydro-simulation helps to validate the former, and motivates us to improve upon the latter by including gas self-gravity, viscosity, turbulence, and dust feedback.

Fast modes promise to better reproduce observed dust distributions with large azimuthal and radial extents (e.g., Casassus et al. 2013; van der Marel et al. 2013). In our demonstration model, particles with sizes of  $0.1$ – $1$  mm have concentration times on the order of the disk age or longer, and should thus occupy horseshoe-shaped regions like those shown in the top right panel of Figure 3. In addition, larger particles, having Stokes parameters  $St \sim 0.1$ – $10$  (particle sizes of  $1$ – $100$  cm), naturally spread themselves in azimuth by  $\sim 45^\circ$ . Gas turbulence can also diffuse dust particles, keeping them on large horseshoe



orbits. The Péclet number is the ratio of timescales for turbulent diffusion and concentration:

$$\text{Pe} \equiv \frac{t_{\text{diff}}}{t_{\text{conc}}} \sim \frac{(\sqrt{16\mu/3} a_0)^2/D}{t_{\text{conc}}} \sim \frac{\text{St}}{\alpha}. \quad (20)$$

Here  $D \approx D_g/(1 + \text{St}^2)$  is the dust particle diffusivity (equation 5 of Youdin & Lithwick 2007),  $D_g \sim \alpha c_s h$  is the gas diffusivity, and  $\alpha < 1$  is the Shakura-Sunyaev turbulence parameter. Small  $\text{Pe} \lesssim 1$  — i.e., more spatially extended dust — obtains for  $\text{St} \lesssim 0.01$  (mm-sized or smaller particles) and  $\alpha \sim 0.01$ .

Our proposed lopsided gas mode is gravitational and global; hence its radial width is not limited by the pressure scale height  $H$ . This limitation afflicts vortices, since the Keplerian shear across a vortex must remain subsonic (e.g., Lithwick 2009; Zhu & Stone 2014). Lyra & Lin (2013) acknowledge this difficulty in the last paragraph of their section 6.5, noting that the radial half-width of the dust trap in Oph IRS 48 is  $17 \text{ AU} \approx 3H$  whereas their vortex theory (see their equation 68) predicts a maximum half-width of  $\sim H/2$ . Our horseshoe-shaped orbits are not constrained by  $H$  and may thus better reproduce the azimuthally and radially wide horseshoe-shaped emission seen in transitional disks like HD 142527 (Casassus et al. 2013). Because the gas mode is global, we speculate that it may be more resistant to the destructive effects of dust back-reaction than are vortices (Johansen et al. 2004; Meheut et al. 2012). Disk gravity underlies our mode but may undercut vortices; Lin & Papaloizou (2011a,b) found that self-gravity shrinks vortices and frustrates their merging.

We have not identified the origin of the fast mode. It may be that, like the vortices of Zhu & Stone (2014), a planet is responsible. A passing star might also pull the disk to one side of the star and excite a long-lived fast mode (see Jalali & Tremaine 2012 who use a passing star to excite slow modes). But for economy of hypothesis, one can do no better than look to the self-gravitational field of the gas disk itself (Dury et al. 2008).

We thank Robin Dong, Mir Abbas Jalali, Eve Lee, Chris Ormel, Roman Rafikov, and Scott Tremaine for useful discussions, and an anonymous referee for an encouraging report. EC acknowledges support from the

Miller Institute and a NASA Origins grant.

## REFERENCES

- Binney, J., Gerhard, O. E., Stark, A. A., Bally, J., & Uchida, K. I. 1991, *MNRAS*, 252, 210
- Brown, J. M., Blake, G. A., Qi, C., Dullemond, C. P., Wilner, D. J., & Williams, J. P. 2009, *ApJ*, 704, 496
- Bruderer, S., van der Marel, N., van Dishoeck, E. F., & van Kempen, T. A. 2014, *A&A*, 562, A26
- Casassus, S., van der Plas, G., M., S. P., Dent, W. R. F., Fomalont, E., Hagelberg, J., Hales, A., Jordán, A., Mawet, D., Ménard, F., Wootten, A., Wilner, D., Hughes, A. M., Schreiber, M. R., Girard, J. H., Ercolano, B., Canovas, H., Román, P. E., & Salinas, V. 2013, *Nature*, 493, 191
- Chang, P., Murray-Clay, R., Chiang, E., & Quataert, E. 2007, *ApJ*, 668, 387
- Chiang, E. & Youdin, A. N. 2010, *Annual Review of Earth and Planetary Sciences*, 38, 493
- Dury, V., de Rijcke, S., Debattista, V. P., & Dejonghe, H. 2008, *MNRAS*, 387, 2
- Espaillet, C., Muzerolle, J., Najita, J., Andrews, S., Zhu, Z., Calvet, N., Kraus, S., Hashimoto, J., Kraus, A., & D'Alessio, P. 2014, *ArXiv e-prints*
- Fukagawa, M., Tsukagoshi, T., Momose, M., Saigo, K., Ohashi, N., Kitamura, Y., Inutsuka, S.-i., Muto, T., Nomura, H., Takeuchi, T., Kobayashi, H., Hanawa, T., Akiyama, E., Honda, M., Fujiwara, H., Kataoka, A., Takahashi, S. Z., & Shibai, H. 2013, *PASJ*, 65, L14
- Isella, A., Pérez, L. M., Carpenter, J. M., Ricci, L., Andrews, S., & Rosenfeld, K. 2013, *ApJ*, 775, 30
- Jalali, M. A. & Tremaine, S. 2012, *MNRAS*, 421, 2368
- Johansen, A., Andersen, A. C., & Brandenburg, A. 2004, *A&A*, 417, 361
- Lin, M.-K. & Papaloizou, J. C. B. 2011a, *MNRAS*, 415, 1445
- . 2011b, *MNRAS*, 415, 1426
- Lithwick, Y. 2009, *ApJ*, 693, 85
- Lovelace, R. V. E. & Romanova, M. M. 2014, *Fluid Dynamics Research*, 46, 041401
- Lyra, W. & Lin, M.-K. 2013, *ApJ*, 775, 17
- Meheut, H., Yu, C., & Lai, D. 2012, *MNRAS*, 422, 2399
- Mignone, A., Bodo, G., Massaglia, S., Matsakos, T., Tesileanu, O., Zanni, C., & Ferrari, A. 2007, *ApJS*, 170, 228
- Murray, C. D. & Dermott, S. F. 1999, *Solar system dynamics*
- Nakagawa, Y., Sekiya, M., & Hayashi, C. 1986, *Icarus*, 67, 375
- Paczynski, B. 1977, *ApJ*, 216, 822
- Pérez, L. M., Isella, A., Carpenter, J. M., & Chandler, C. J. 2014, *ApJ*, 783, L13
- Pérez, S., Casassus, S., Ménard, F., et al. 2014, *arXiv:1410.8168*
- Tang, Y.-W., Guilloteau, S., Piétu, V., Dutrey, A., Ohashi, N., & Ho, P. T. P. 2012, *A&A*, 547, A84
- Tremaine, S. 2001, *AJ*, 121, 1776
- van der Marel, N., van Dishoeck, E. F., Bruderer, S., Birnstiel, T., Pinilla, P., Dullemond, C. P., van Kempen, T. A., Schmalzl, M., Brown, J. M., Herczeg, G. J., Mathews, G. S., & Geers, V. 2013, *Science*, 340, 1199
- Youdin, A. N. & Lithwick, Y. 2007, *Icarus*, 192, 588
- Zhu, Z. & Stone, J. M. 2014, *ArXiv e-prints*